# Demonstration of LDPC-Coded PS-64QAM OFDM Employing a Novel Bit-Class Distribution Matching in W-band ROF system

**Haitao Zhao (赵海涛) [1], Bangning Xu (徐邦宁) [1], Wei Xun (荀位) [1], Jianxin Ren (任建新) [2], Shuaidong Chen (陈帅东) [2], Long Zhang (张龙) [3], Li Zhao (赵利) [1,3], Bo Liu (刘博) [2,*]**

[1] School of communication and information engineering, Nanjing University of Posts and Telecommunications

[2] Institute of Optics and Electronics, Nanjing University of Information Science & Technology, Nanjing 210044, China

[3] Key Laboratory for Information Science of Electromagnetic Waves (MoE), Fudan University, Shanghai 200433, China

*Corresponding author: bo@nuist.edu.cn

Received Month X, XXXX; accepted Month X, XXXX; posted online Month X, XXXX

In this work, we proposed and experimentally demonstrated a novel probabilistic shaping (PS) 64-ary quadrature amplitude modulation (QAM) orthogonal frequency division multiplexing (OFDM) with low-density parity-check (LDPC)-coded modulation in a W-band RoF system using envelope detection. The proposed PS scheme has the advantages of no complex multiplication and division operations and low hardware implementation complexity. In our experiments, the two-stage bit weight distribution matching-based PS-64QAM OFDM signals with a rate of 28.13-Gb/s transmission over 4-m wireless + 45-km SSMF transmission can be achieved. The system performance is investigated under one LDPC code rates (3/4) and two PS parameter values (k=3 and 9). The experimental results show that the receiver power sensitivity and the system fiber nonlinear effect tolerance can be significantly improved compared with uniformly-distributed OFDM signals.

**Keywords**: Probabilistic Shaping, two-stage bit weight distribution matching, OFDM, W-band RoF.
DOI: 10.3788/COLXXXXXX.XXXXXX.

## 1. Introduction

The advent of 5G technology has resulted in an exponential increase in mobile traffic data and increased demands on mobile networks due to the development of new technologies like augmented reality, smart healthcare, drones [1]. Because of its considerable advantages over rivals, Centralized/Cloud Radio Access Network (C-RAN) architecture has improved its ability to respond to market conditions in recent years. In [2] The Baseband Units (BBUs), which are centralized in a single site or even in the cloud, are kept apart from the system's Remote Radio Heads (RRHs) via the C-RAN technique. This method increases the demands for high speed, low latency, and precise synchronization on the network connection between the RRHs and BBUs while simultaneously lowering the cost of equipment and making radio unit layout less complicated. These crucial needs can be satisfied by mobile front-end (MFD) networks based on radio-over-fiber (RoF) [3]. But not every location is appropriate for the deployment of fiber. The fiber deployment is expensive in hilly and metropolitan locations. As a result, developing radio access networks (RANs) with high communication capacity, high flexibility, and cheap engineering cost has drawn attention. The advantages of millimeter wave (MMW) transmission include a broad frequency range and very little air attenuation. For high-speed RoF transmission that goes beyond sub-6G, this frequency range is perfect. It has been claimed several times [4-5] that photonics-aided W-band long-distance high-speed communication can provide flexible transmission for MFD customers in the last mile. W-band (75~110 GHz) radio, in particular, provides high precision and low air attenuation. As a result, a W-band RoF system can increase the transmission range and capacity of wireless services [6-8]. However, the bulk of MMW-RoF techniques now in use rely on expensive and intricate coherent receivers to transmit signals [9]. In addition to avoiding complicated and expensive high-speed mixers, millimeter-wave local oscillators, and high-speed DACs in order to save equipment costs, the intensity modulation and direct detection (IM-DD) schemes using envelope detector (ED) also prevent frequency drift in the photon-assisted MMW system [10].

Furthermore, the probabilistically shaped (PS) constellation may be utilized for rate adaptation and is viewed as a promising way to escape Shannon's limit [11]. Recently, the Gallager many-to-one mapping (MTO), the hierarchical distribution matcher (HiDM), the constant composition distribution matcher (CCDM), the bit-weighted distribution matching (BWDM), and the prefix-

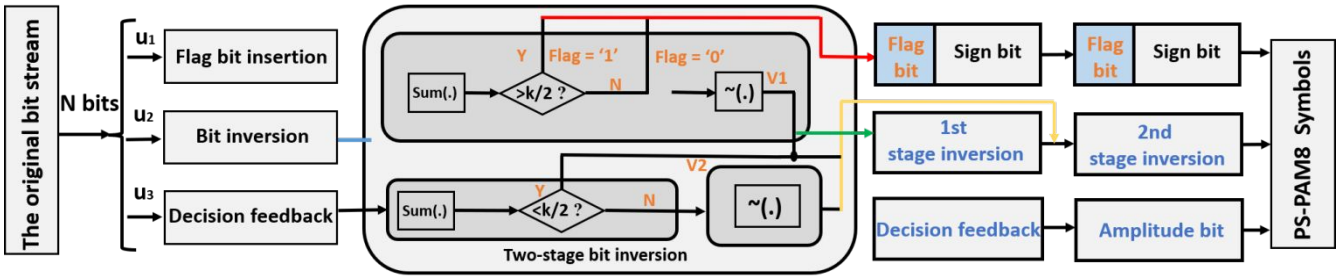


Fig. 1. Principle flowchart for two-stage bit weight distribution matching.

free code distribution matching (PCDM) are a few PS approaches that have been presented [12-14]. Only PCDM, BWDM, and HiDM have had FPGA implementations [13-15]. To employ the MTO shaping technique, the receiver must design an iterative strategy that applies both inner and outer iterations to the low-density parity-check (LDPC) decoder and the PS decoder. This demonstrates that the technique is costly in terms of computation time, memory utilization, power consumption, and hardware implementation complexity. Furthermore, the CCDM requires resource-intensive division and multiplication operations [16]. In [17], a low-complexity PS-16QAM scheme based on BWDM for OFDM symbols in an IM-DD system is presented. L. Zhang et al. demonstrated it in a high-speed real-time system [15]. The experimental results show that the system does not require complicated multiplication and division operations, and thus has reduced computational and hardware complexity. The shortcoming of this method is that it cannot be used directly to higher order 64-ary quadrature amplitude modulation (QAM).

In this work, we propose and experimentally demonstrate a novel PS-64QAM-OFDM based on two-stage bit weight distribution matching (TS-BWDM) for an IM-DD-based W-band RoF system. The signal is transmitted over 45-km standard single-mode fiber (SSMF) and 4-m wireless links. Compared with the high-cost coherent, the system uses one low-cost W-band ED to restore the received signals to baseband. After 45-km SSMF and 4-m wireless transmission, 28.13 Gb/s PS-64QAM-OFDM signal transmission is obtained with BER smaller than $2.2\times10^{-2}$. The experimental results show that the TS-BWDM-based PS-64QAM

## 2. Operation Principle

The process of TS-BWDM in detail is depicted in Fig. 1. Firstly, the original input bit stream is divided into three parallel data streams, $U_1$, $U_2$ and $U_3$ with the matching bit length of $n_1$, $n_2$ and $n_3$ following the serial to parallel conversion. Here, $U_1$-path performs flag bit insertion, $U_2$-path mainly realizes two-stage bit-weighted inversion, and $U_3$-path performs the judgment of the second bit-weighted inversion to realize approximate Gaussian distribution (GD). The three parallel data streams can be expressed as

$$U_i = \left\{ D_{i,1},\ D_{i,2},\ \ldots,\ D_{i,n_i} \right\} \tag{1}$$

where $D \in \{0,1\}$ and $i$ is the index of the parallel bit streams. The $U_2$ is then subjected to the two-stage bit-weighted inversion processing procedure, which is a crucial component of TS-BWDM. In the two-stage bit-weighted inversion, $U_2$ is bitwise separated into a number of sets, each of which contains $k$ bits, and one flag bit, the newly added most significant bit (MSB), is added to $U_1$ set via weight computation based on the original k elements of $U_2$. The constellation labeling design with Gray mapping rules for PS-PAM8 is shown in Fig. 2(a). The yellow marked bit represents the symbol bit. It is obvious that the PS can be achieved by increasing the probability of '1' in the inner circle of $U_2$. After the weight calculation, if the probability of '1' is greater than k/2, the corresponding MSB is defined as '1'. If not, the MSB is set to '0' and the $k$ bits of the set undergo a bit negation operation.

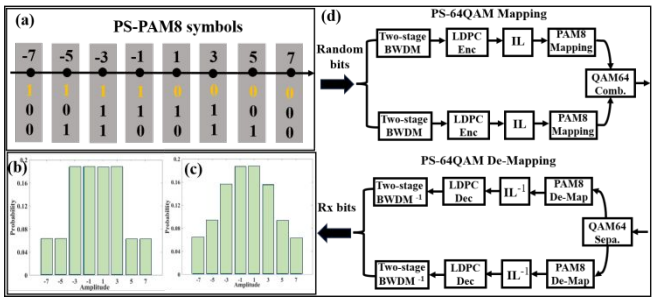


Fig. 2. (a) PS-PAM8 with Gray mapping, (b) and (c) The probability distribution constellation example of $k = 3$ for 1st stage inversion and 2st stage inversion (d) The process of LDPC-coded PS-64QAM Mapping/De-Mapping.

Fig.2 (b) shows the probability distribution of PS-PAM8 symbols for $k$=3 after 1st stage inversion. To achieve the PS-PAM8 signals following approximate GD, similarly, the $U_3$ is divided into several sets according to the flag bits inserted by the first bit-weighted reversion operation, and each set also includes k bits. After calculating the weight of the subset in $U_3$, the bits in the subset of $U_2$ corresponding to '1' in the subset of $U_3$ are subject to the bit inversion operation if the probability of '1' is greater than $k$/2. If not, these bits remain unchanged. It is worth noting that the two-stage bit-weighted inversion here are performed on $U_2$, and only one-stage flag bit insertion operation is performed on $U_1$. By the first stage bit-weighted inversion processing procedure, the probabilities of '1' and '0' in the $U'_2$ can be written as

$$P(U'_2)=\begin{cases}\dfrac{1}{2^k}\left(\sum\limits_{x=\lceil k/2\rceil}^{k}\dfrac{x+1}{k+1}C_k^x+\sum\limits_{x=\lfloor k/2\rfloor+1}^{k}\dfrac{x}{k+1}C_k^x\right), & U'_2=1\\ 1-\dfrac{1}{2^k}\left(\sum\limits_{x=\lceil k/2\rceil}^{k}\dfrac{x+1}{k+1}C_k^x+\sum\limits_{x=\lfloor k/2\rfloor+1}^{k}\dfrac{x}{k+1}C_k^x\right), & U'_2=0\end{cases} \tag{2}$$

where $\lceil g \rceil$ means the operation for the minimal integer larger than the value inside it. $\lfloor g \rfloor$ indicates the opposite operation.

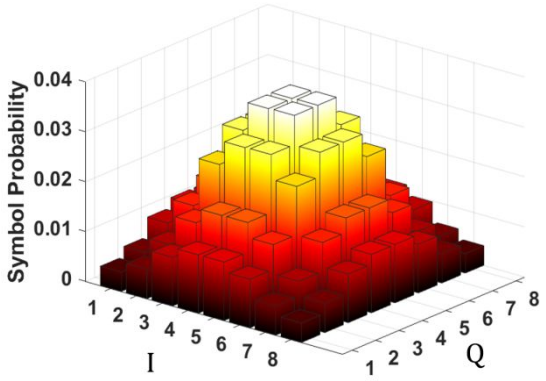


Fig. 3. The probability distribution of PS-64QAM symbols.

The key to the second stage bit-weighted reversion is to re-reverse the subset in $U'_2$ according to the distribution of '1'and '0' in $U'_3$, which includes three steps: (1) The flag bits added by the initial bit-weighted reversion operation are used to partition the $U'_3$ into a number of sets, each of which also contains k bits. (2) Calculate the weight of the subset in $U'_3$. (3) Find the bits in the subset of $U'_2$ corresponding to '1' in the subset of $U'_3$, if Z is greater than $k/2$, and these found bits is re-reversed. If not, these bits remain unchanged. The probability distribution of PS-PAM8 symbols for $k$=3 after second stage inversion is shown in Fig. 2(c). The detail LDPC-coded PS-64QAM based on two-stage BWDM generation procedure is shown in Fig. 2(d). After 64QAM mapping operation, the generated PS-64QAM constellation is shown in Fig. 3.

The mutual information (MI) of the modulated signal for a N-order order constellation set X transmitted in the additive Gaussian white noise (AWGN) channel can be represented by

$$\begin{aligned}\mathrm{I}(X;Y)&=H(Y)-H(Y/X)=H(X+N)-H(N)\\&=\sum_{x\in X}\sum_{y\in Y}p(x,y)\log\frac{p(x,y)}{p(x)p(y)}\\&=\sum_{x}p(x)\left[\sum_{y}p(y/x)\log p(y/x)\right]\\&\quad-\sum_{y}\log p(y)\sum_{x}p(x,y)\\&=-\sum_{x}p(x)H(Y/X=x)-\sum_{y}\log p(y)p(y)\end{aligned} \tag{3}$$

where $p(y/x)$ and H(.) indicate the conditional transition probability density and the information entropy, respectively. It is feasible to communicate reliably across the AWGN channel if the transmission rate per real dimension does not exceed the channel capacity C. It can be written as

$$C=\max \mathrm{I}(X;Y) \tag{4}$$

Fig. 4 illustrates the channel capacity for uniformly-distributed 64QAM (UD-64QAM) and TS-BWDM-based PS-64QAM in the cases of k = 3, respectively. Obviously, approximately 0.61-dB shaping gain can be correspondingly obtained in the cases of k=3, compared with the UD-64QAM. Additionally, in the case of k=3, 5, and 9, the net rate of BWDM-based PS-16QAM is 5.76, 5.88 and 5.93 bits/symbol regardless of FEC redundancy.

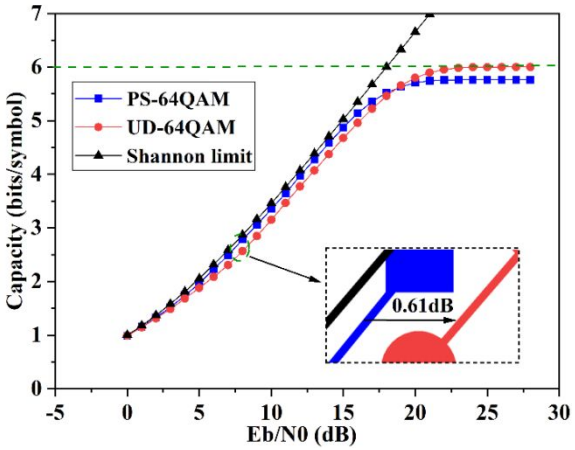


Fig. 4. Theoretical analysis of channel capacity.

Table1. Some Key Parameters Used in the Experiment

| Parameter | Value |
|---|---|
| Modulation format | 64QAM |
| FFT/IFFT Size | 1024-point |
| Data-SCs | 400 |
| CP length | 32-point |
| OFDM symbols per frame | 243 |
| TS | 5 |
| Digital clipping ratio | 12-dB |
| $k$ (PS) | 3 / 9 |
| LDPC code length and rate | 48600 / 3/4 |

## 3. DSP and Experimental Setup

Fig. 5 shows the experimental setup of the LDPC-coded PS-64QAM OFDM for IM-DD-based W-band RoF system. At the transmitter, the modulated signal is sent to AWG (Tektronix AWG7122C). After then, the MZM (FTM7938EZ) is driven by this data sequence. With the bias voltage adjusted to -4.5 V, the MZM functions close to the quadrature point. The signal amplitude stays within the linear driving voltage range of MZM. Two external

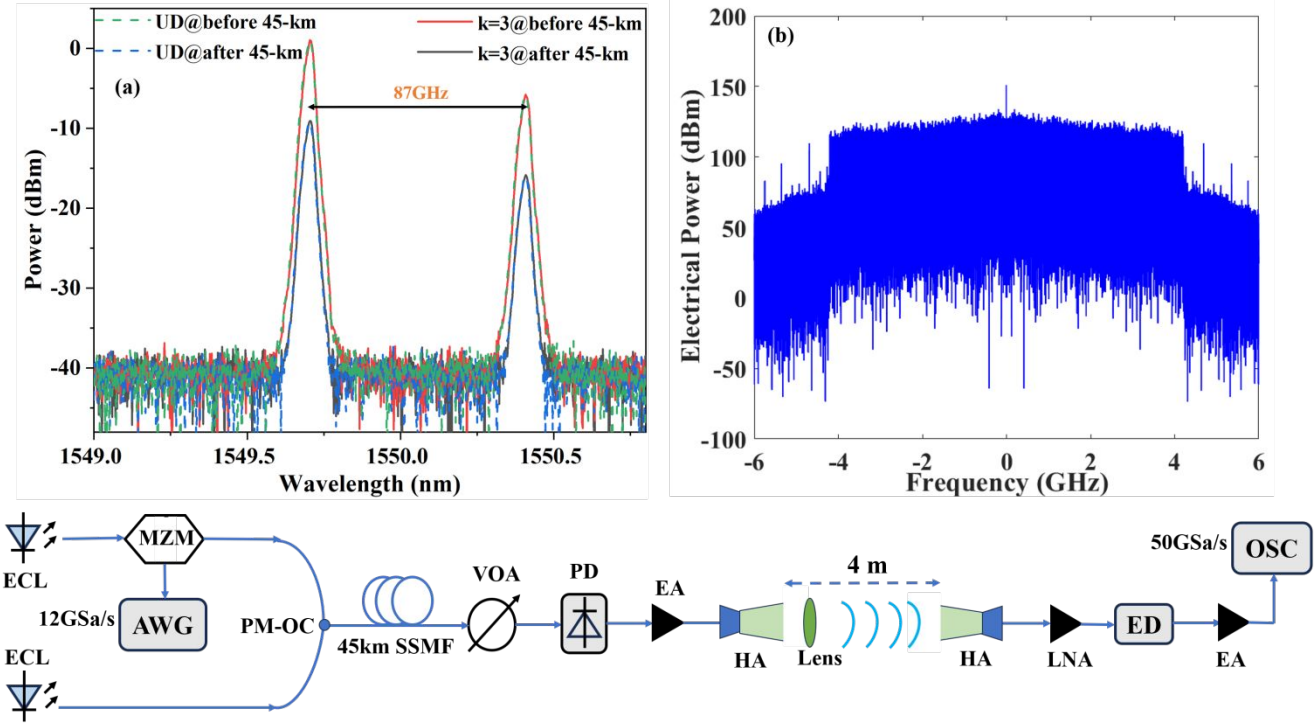


Fig. 5. Experimental setup. Insets (a) The measured optical spectrum after the OC processing, (b) The electrical spectra for PS - 64QAM OFDM.

cavity lasers with 100 kHz linewidth produce beams at 1550 nm and 1550.7 nm with a channel spacing of 87 GHz. The modulator has an insertion loss of 9 dB and combines the two laser beams via polarization-maintaining optical coupler (PM-OC) before sending them to the MZM as an optical carrier. A range of 0 dBm to 3 dBm is maintained for the optical power prior to PD detection. The light waves are combined by the PM-OC with optical spectrum in Fig. 5(a). The optical signal is square-law detected by the 50 GHz bandwidth PD (XPDV21), which then modulates the signal onto the 87 GHz center carrier. The W-band signal is sent to free space via a horn antenna with a gain of 25 dBi after being amplified by an electrical amplifier (EA) operating at 75 GHz~100 GHz with a gain of 21 dB. The MMW signal is down-converted to the baseband OFDM signal through the envelope detector via 45-km SSMF and 4-m wireless propagation and amplified by a horn antenna with a gain of 25 dBi, a lens with a gain of 15 dBi, and a W-band LNA with a gain of 30 dB. After being amplified by an EA with a gain of 30 dB, the signal is captured offline by a real-time oscilloscope operating at a sampling rate of 50 GSa/s and a bandwidth of 16GHz. Fig. 5(a) illustrates the electrical spectrum of the PA-64QAM OFDM signal.

Figs. 6(a) and 6(b) show the DSP at the transmitter and the receiver, respectively. The IFFT size is 1024 and 400 subcarriers are loaded with data. The length of both the cyclic prefix and suffix is 32. The ISFA taps is 4. One OFDM frame comprises of 9 TSs and 243 data-carrying OFDM symbols. The bandwidths of LDPC-coded UD-64QAM, PS-64QAM OFDM signal k=9) and that of k=3 are about 4.18 GHz, 4.34 GHz and 4.69 GHz, respectively. The LDPC code length and rate is 46800 and 3/4 in our experiment. Here, the binary data after parallel-to-serial conversion are used to generate 64800 bits per LDPC block via the FEC encoder in consideration of the cooperation with LDPC codes for more dependable transmission. The maximum number of iterations is 30. The decoder for LDPC codes is belief propagation decoding algorithm. Here, the belief propagation decoding algorithm and a maximum of 30 iterations is used to decode the logarithmic likelihood ratio.

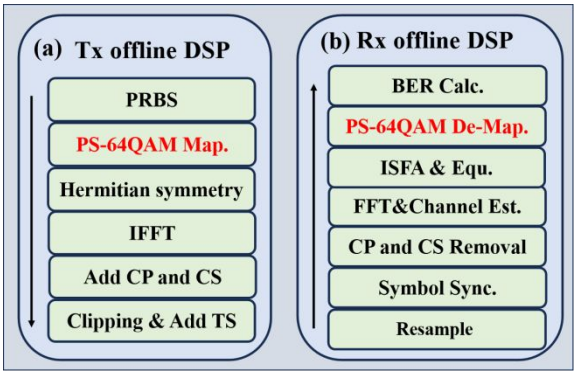


Fig. 6. Block diagram of PS-64QAM OFDM system.

## 4. Results and Discussion

Fig. 7 shows the estimated SNR across the data subcarriers index for the PS-64QAM OFDM with k=3. The ISFA-enhanced channel estimation method can provide more accurate channel estimation for subcarriers and achieve improved SNR performance.

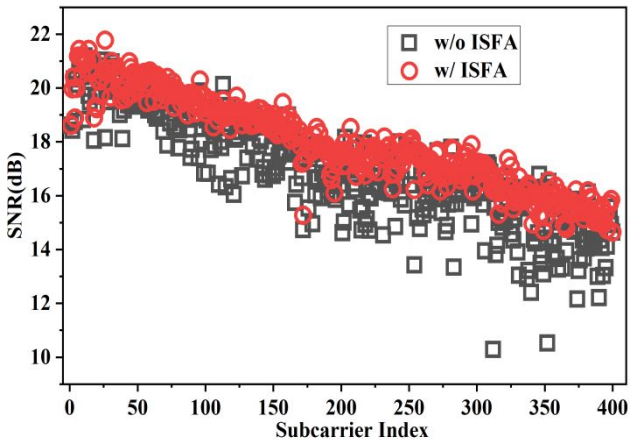


Fig. 7. The SNR versus subcarrier index for PS-64QAM OFDM after 4-m wireless and 45-km SSMF transmission.

Fig. 8 shows the BER performance for UD/PS-64QAM OFDM signals over 4-m wireless transmission. For fair comparison, the bit rates of all three signals (UD, k=3 and k=9) are 28.13Gb/s. For the post-FEC BER performance, the received optical power (RPS) improvement for k=3 and k=9 signals after 4-m wireless transmission are 0.97 and 0.48dB compared with the UD-64QAM at the BER of $2.2\times10^{-5}$, respectively. The insets (a), (b) and (c) in Fig. 8 show the recovered constellation diagrams of OFDM for the three cases of UD, k = 9 and k = 3, respectively.

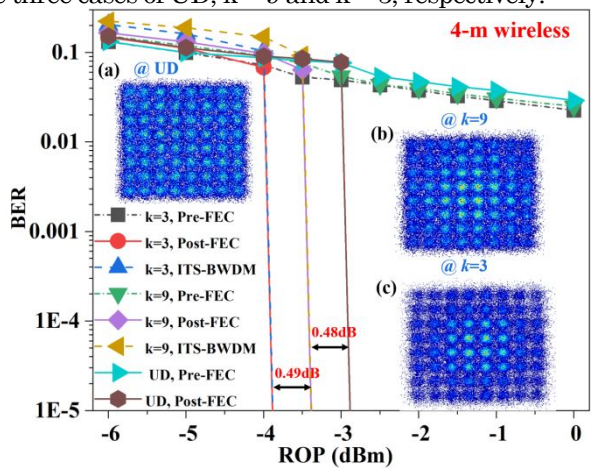


Fig. 8. BER versus ROP at 4-m wireless transmission.

According to the result of the 4-m wireless transmission experiment, we carried out the 4-m wireless + 45-km SSMF transmission experiment of UD/PS-64QAM OFDM. Fig. 9 illustrates the BER performance of UD/PS-OFDM versus different ROPs over 45-km SSMF + 4-m wireless. Compared with UD-OFDM, PS-OFDM with k=3 and 9 can reach the BER of $2.4\times10^{-2}$. In addition, the receiver sensitivities of the PS-OFDM receivers with k =3 in terms of ROP can be improved by more than 1.4 dB at the BER of $1.8\times10^{-5}$ compared to UD-OFDM. The reduced signal average power by PS technique, which may lessen the harm on the transmitted signal produced by the fiber nonlinear effect, can benefit both the IM/DD and the coherent detection systems with negative electrical field [18]. The reconstructed constellation diagrams of OFDM for the three situations of UD, k=9 and 3, are displayed in the insets (a), (b), and (c) of Fig. 9, respectively. In Figs. 8-9, the post-FEC is referring to after LDPC decode and without ITS-BWDM.

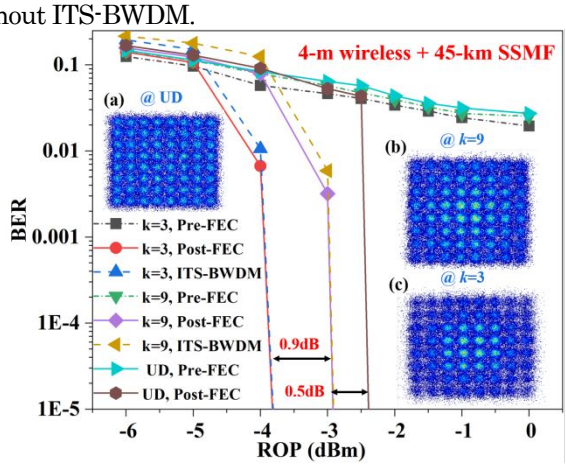


Fig.9. BER versus ROP at 45-km SSMF + 4-m wireless transmission.

## 4. Conclusion

In conclusion, a novel probabilistic shaping (PS) 64QAM-OFDM with LDPC-coded modulation in a W-band RoF system using envelope detection is proposed and experimentally demonstrated. The proposed PS scheme has the advantages of no complex multiplication and division operations and low hardware implementation complexity. Apart from shaping gain, the PS-64QAM OFDM signal outperforms the UD-64QAM OFDM signal in terms of receiver power sensitivity and fiber nonlinear effect tolerance. The power sensitivity of the optical receiver in the experiment has increased by at least 1.4 dB higher than that of UD, according to the experimental data.

**Funding Sources.** This work was supported by Natural Science Research Start-up Foundation of Recruiting Talents of Nanjing University of Posts and Telecommunications (Grant No. NY223144)

## References.

1. Vaezi et al., "Cellular, wide-area, and non-terrestrial IoT: A survey on 5G advances and the road toward 6G," IEEE Commun. Surveys Tuts., vol. 24, no. 2, pp. 1117–1174, 2nd Quart., 2022, doi: 10.1109/COMST.2022.3151028.
2. . Breyne, G. Torfs, X. Yin, P. Demeester, and J. Bauwelinck, "Comparison between analog radio-over-fiber and sigma delta modulated radioover-fiber," IEEE Photon. Technol. Lett., vol. 29, no. 21, pp. 1808–1811, Nov. 1, 2017, doi: 10.1109/LPT.2017.2752284.
3. S. Liu, X. Wang, W. Zhang, G. Shen, and H. Tian, "An adaptive activated ANN equalizer applied in millimeter-wave RoF transmission system," IEEE Photon. Technol. Lett., vol. 29,

no. 22, pp. 1935–1938, Nov. 15, 2017, doi: 10.1109/LPT.2017.2753174.
4. . Wang et al., “Delivery of polarization-division-multiplexing wireless millimeter-wave signal over 4.6-km at W-band,” J. Lightw. Technol., vol. 40, no. 19, pp. 6339–6346, Oct. 1, 2022, doi: 10.1109/JLT.2022.3195542.
5. J. Yu, X. Li, W. Zhou, "Tutorial: Broadband fiber-wireless integration for 5G+ communication", APL Photonics. 3, 111101 (2019).
6. X. Li, J. Yu, and G.-K. Chang, “Photonics-assisted technologies for extreme broadband 5G wireless communications,” J. Lightw. Technol., vol. 37, no. 12, pp. 2851–2865, Jun. 15, 2019.
7. B. Zhu, Y. Wang, W. Li, F. Wang, J. Liu, M. Kong, and J. Yu, "Delivery of 40 Gbit/s W-band signal over 4600 m wireless distance employing advanced digital signal processing", Chin. Opt. Lett. 20, 103901 (2022).
8. X. Li, J. Yu, L. Zhao, K. Wang, C. Wang, M. Zhao, W. Zhou, J. Xiao, "1-Tb/s millimeter-wave signal wireless delivery at D-band", J. Lightwave Technol. 37, 196 (2019).
9. Y. Li, J. Yu, R. Song, and N. Liu, "D-band signal generation and transmission without optical filter based on optical carrier suppression and single-sideband modulation", Opt. Express. 30, 436 (2022).
10. J. He, Z. Zhou and J. He, "A rotated QAM-based probabilistically shaped OFDM with ANN scheme for W-band RoF system", 2022 Optical Fiber Communications Conference and Exhibition (OFC), pp. 1-3, 2022.
11. T. Fehenberger, A. Alvarado, G. Böcherer, and N. Hanik, “On probabilistic shaping of quadrature amplitude modulation for the nonlinear fiber channel,” J. Light. Technol., vol. 34, no. 21, pp. 5063–5073, 2016.
12. Z. Cao, Y. Chen, X. Zhao, L. Zhou, and Z. Dong, “Probabilistic Shaping 44QAM Based on Many-to-One Mapping in DMT-WDM-PON,” IEEE Photon. Technol. Lett. 32(11), 639–642 (2020).
13. Q. Yu, S. Corteselli, and J. Cho, “FPGA implementation of rate-adaptable prefifix-free code distribution matching for probabilistic constellation shaping,” J. Lightw. Technol., vol. 39, no. 4, pp. 1072–1080, Feb. 2021.
14. L. Zhang, K. Tao, W. Qian, W. Wang, J. Liang, Y. Cai, and Z. Feng, “Real-time FPGA investigation of interplay between probabilistic shaping and forward error correction,” J. Lightw. Technol., vol. 40, no. 5, pp. 1339–1345, 2022.
15. L. Zhang, K. Wang, C. Wang, "Real-time demonstration of a low-complexity PS scheme for 16QAM-DMT signals in an IM-DD system", *Opt. Exp.*, vol. 31, no. 7, pp. 11447-11456, 2023.
16. P. Schulte and G. Böcherer, “Constant composition distribution matching,” IEEE Trans. Inf. Theory, vol. 62, no. 1, pp. 430–434, Jan. 2016.
17. Z. Dong, Y. Chen, D. Zou, X. Zhao, L. Zhou, and F. Li, “DMT transmission in short-reach optical interconnection employing a novel bit-class probabilistic shaping scheme,” J. Lightwave Technol. vol. 39, no. 1, pp. 98–104, 2021.
18. J. Yu, K. H. Wang, J. W. Zhang, B. Y. Zhu, “8×506-Gb/s 16QAM WDM signal coherent transmission over 6000-km enabled by PS and HB-CDM,” in Proc. Opt. Fiber Commun. Conf. Expo. (OFC), USA, Mar. 2018, Paper M2C.3.